Repeated Eyewall Replacement Cycles in Hurricane Frances (2004)

JOHN MOLINARI

Department of Atmospheric and Environmental Sciences, University at Albany, State University of New York, Albany, New York

JUN A. ZHANG

Hurricane Research Division, NOAA/AOML, and Cooperative Institute for Marine and Atmospheric Studies, University of Miami, Miami, Florida

ROBERT F. ROGERS

Hurricane Research Division, NOAA/AOML, Miami, Florida

DAVID VOLLARO

Department of Atmospheric and Environmental Sciences, University at Albany, State University of New York, Albany, New York

(Manuscript received 25 September 2018, in final form 12 March 2019)

ABSTRACT

Hurricane Frances (2004) represented an unusual event that produced three consecutive overlapping eyewall replacement cycles (ERCs). Their evolution followed some aspects of the typical ERC. The strong primary eyewalls contracted and outward-sloping secondary eyewalls formed near 3 times the radius of maximum winds. Over time these secondary eyewalls shifted inward, became more upright, and replaced the primary eyewalls. In other aspects, however, the ERCs in Hurricane Frances differed from previously described composites. The outer eyewall wind maxima became stronger than the inner in only 12 h, versus 25 h for average ERCs. More than 15 m s^{-1} outflow peaked in the upper troposphere during each ERC. Relative vorticity maxima peaked at the surface but extended to mid- and upper levels. Mean 200-hPa zonal velocity was often from the east, whereas ERC environments typically have zonal flow from the west. These easterlies were produced by an intense upper anticyclone slightly displaced from the center and present throughout the period of multiple ERCs. Inertial stability was low at almost all azimuths at 175 hPa near the 500-km radius during the period of interest. It is hypothesized that the reduced resistance to outflow associated with low inertial stability aloft induced deep upward motion and rapid intensification of the secondary eyewalls. The annular hurricane index of Knaff et al. showed that Hurricane Frances met all the criteria for annular hurricanes, which make up only 4% of all storms. It is argued that the annular hurricane directly resulted from the repeated ERCs following Wang's reasoning.

1. Introduction

The work of Willoughby et al. (1982) and Black and Willoughby (1992) established the existence of distinctive eyewall replacement cycles in tropical cyclones. A strong primary eyewall contracts as a storm intensifies, but before maximum intensity is reached a second eyewall occasionally forms some distance outside the first. Over time the outer eyewall can either induce subsidence over the inner eyewall or rob the inner eyewall of inflow, which instead ascends at larger radii. The inner eyewall weakens as a result, and eventually vanishes. At the same time, the outer eyewall wind maximum, vorticity, and convection grow stronger. The outer eye contracts and a new deepening cycle begins. The term eyewall replacement cycle (ERC) has been used to describe this sequence of events. The eyewall contractions (both inner and outer) arise because a ring of convection will produce maximum increases in cyclonic wind just inside of the radius of maximum heating,

Corresponding author: John Molinari, jmolinari@albany.edu

DOI: 10.1175/MWR-D-18-0345.1

resulting in an inward shift of the eyewall (Shapiro and Willoughby 1982; Pendergrass and Willoughby 2009). Initially the outer eyewall might be a trailing spiral, but vorticity axisymmetrization acts to produce a circular feature over time (e.g., Guinn and Schubert 1993).

Sitkowski et al. (2011, hereafter SKR11) used 31 years of flight-level data to examine 24 ERC events in 14 hurricanes. ERCs occurred most often in major hurricanes. More than half of the storms examined produced only a single ERC event. SKR11 developed a composite evolution of an ERC, which was divided into three phases lasting, on average, 36 h. The first phase began with the initial appearance of an outer wind maximum (t_0) and continued as the inner eyewall kept contracting and strengthening until t_0 + 9 h. During the second phase, the storm weakened as a secondary eyewall formed, and by t_0 + 25 h this outer wind maximum was as intense as the primary. The strengthening of the outer wind maximum and weakening of the inner eyewall continued during the last phase. By t_0 + 36 h, the inner wind maximum could no longer be detected and the ERC was defined as complete. This schematic showed the mean evolution, but the structure and behavior of individual ERCs did not always follow the idealized sequence above.

In the presence of moderate vertical wind shear, Didlake et al. (2017) described asymmetric double eyewalls. The outer eyewall was shifted cyclonically with azimuth from the inner one. Dougherty et al. (2018) found similar asymmetries in Hurricane Bonnie (1998) in the presence of large vertical wind shear. Virtually no intensity change occurred despite a well-defined ERC. The recent literature thus reveals that ERCs are influenced by many factors and exhibit a complex range of behavior, the full extent of which is unknown.

One fundamental question has not been fully resolved: what causes the outer eyewall to develop? Several theories exist. Montgomery and Kallenbach (1997) identified vortex Rossby waves (VRWs) that propagated outward on the tropical cyclone radial potential vorticity gradient in the form of trailing spirals. At about 3 times the radius of maximum winds (RMWs), these waves reached a stagnation radius and accumulate cyclonic angular momentum. The authors argued that secondary eyewalls could form by this process in mature hurricanes. Corbosiero et al. (2006) described a sequence of events of azimuthal wavenumber-2 Rossby waves that supported the theory of Montgomery and Kallenbach (1997). Such waves are difficult to see in observations; Corbosiero et al. (2006) used radar reflectivity over several hours with 5-min temporal and 750-m spatial resolution over 150 km of radius to identify these features. A numerical simulation by Abarca and Corbosiero (2011) made similar arguments on the role of Rossby waves on ERCs. In principle, this process could create a secondary eyewall because the increase in cyclonic flow from the momentum accumulation can enhance surface fluxes, convection, and cyclonic vorticity. The mechanism does not require any external forcing. It is striking that SKR11 found mean inner and outer eyewall radii of 35 and 106 km, respectively, consistent with the factor of 3 predicted by the theory.

Terwey and Montgomery (2008), Cotto et al. (2015), and Gonzalez et al. (2015) argued for VRW influence on secondary eyewall formation both in theory and in idealized models. They noted that a broad decrease in axisymmetric vorticity with radius was sufficient for VRW propagation. This VRW mechanism could in principle be forced by convective oscillations in the eyewall and not require external forcing.

Considerable controversy exists as to whether the boundary layer processes in the outer eyewall are balanced or unbalanced (Rozoff et al. 2012; Huang et al. 2012; Kepert 2013; Abarca and Montgomery 2014, Abarca and Montgomery 2015; Wu et al. 2016), but there is little doubt that the resulting contracting outer eyewall is based in the boundary layer.

An alternative set of mechanisms for ERC initiation have been proposed that differ dramatically from the above papers: those excited by external forcing. Molinari and Vollaro (1989; p. 1104) argued that interaction with an upper-level midlatitude trough produced midlevel spinup outside the core driven by lateral eddy flux convergence of angular momentum. They showed that this induced upward motion at outer radii and initiated an eyewall cycle. Similar arguments were made concerning external forcing by Nong and Emanuel (2003).

Dai et al. (2017) attributed an ERC to a storm experiencing increasing vertical wind shear as it approached a westerly jet. When the jet was removed, the ERC did not occur. Didlake and Houze (2011) and Didlake et al. (2017) analyzed secondary eyewall formation originating from asymmetric spiral rainbands for storms in moderate vertical shear environments. They postulated a role for stratiform band inflow downdrafts reaching the surface and feeding the growing secondary eyewall as a result of convergence and acceleration of the tangential wind.

Dougherty et al. (2018) described a secondary eyewall in Hurricane Bonnie (1998). They described the existence of external forcing as exceptionally large vertical wind shear over warm water produced strong outer bands downshear. These bands, initially asymmetric,

wrapped almost all the way around the storm at the secondary eyewall radius. The lack of even a single $5\,m\,s^{-1}$ change in Hurricane Bonnie's intensity over 72 h during the ERC was remarkable. The unusual behavior of Hurricane Bonnie suggests that secondary eyewalls seem to have multiple formation mechanisms and a wide range of behavior thereafter. Both internal and external factors can coexist (Nong and Emanuel 2003) and act in concert or opposition.

Hurricane Frances (2004) exhibited unusual behavior: three full eyewall replacement cycles occurred over a 6-day period. SKR11 described only two events where more than three cycles occurred in a single storm, and in only one of those were the ERCs overlapping. The current study addresses the structure and evolution of the eyewalls in Hurricane Frances and the possible reasons for its unusual behavior.

2. Data and methods

The eyewall replacement cycles in Hurricane Frances will be defined in this paper by ARCHER "ring score" profiles (Wimmers and Velden 2016; Wimmers et al. 2017, 2018). This procedure defines ring structures in microwave data in tropical cyclones, and the rings are plotted in a radius–time Hovmöller diagram. The ring scores are also part of an experimental ERC prediction program (M-PERC[1]; see Kossin and DeMaria 2016). These methods provide an outstanding picture of the evolution of eyewall replacement cycles for real-time analysis, as will be seen later in Fig. 1.

Data obtained from USAF and NOAA P-3 flights between 30 August and 2 September 2004 were utilized in this study. The USAF C-130 typically flew in the early morning hours while the NOAA P-3 missions were in the late afternoon, resulting in an approximate 12-h time separation of the data during the study period. From 31 August to 2 September the USAF flew an additional afternoon mission which closely overlapped with the NOAA P-3. Data from both aircraft were combined for these periods. In total, there were 11 individual flights spanning two complete ERCs. Radially binned, quality controlled values of flight-level wind were available with 0.1-km resolution from the FLIGHT+ dataset (Vigh et al. 2018). The θ_e was calculated only from P-3 flights; the USAF was missing necessary data.

A table will be shown of composite values of various parameters determined by Kossin and Sitkowski (2009, hereafter KS09) during eyewall replacement cycles. KS09 did not publish those values; rather, J. Kossin provided them for the paper by Dougherty et al. (2018). We will refer to KS09 as the source for these values, but note that Table 2 and Fig. 6 in Dougherty et al. (2018) actually list them.

Additional information was gleaned through processing the tail radar from the NOAA P-3 during flights B, D, F1, and H2 (see Table 1). Dual-Doppler winds from this radar made use of Gamache and Marks's (1997) automated variational algorithm. Solving the radar projection equations and continuity equation, solutions from Gamache and Marks's (1997) algorithm

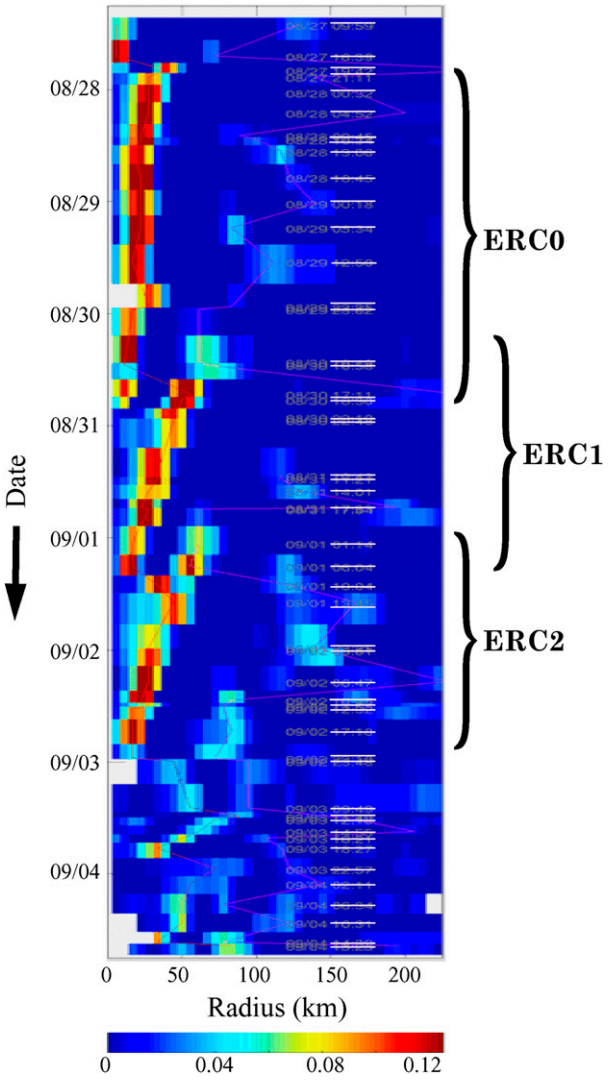

FIG. 1. Hovmöller diagram of the ARCHER ring score following the procedures of Wimmers et al. (2017). The initiation of an outer eyewall is indicated beginning at the green shading. The light line segments on the right half of the panel indicate the times of microwave observations entering the calculation. The three eyewall replacement cycles are indicated by ERC0, ERC1, and ERC2. The dates on the vertical axis are at 0000 UTC.

[1] http://tropic.ssec.wisc.edu/real-time/archerOnline/web/index_erc.shtml

TABLE 1. List of flights used to study Hurricane Frances. Three sets of overlapping flights were combined. Thus the same central time is listed covering both flights. Also shown is the storm intensity from HURDAT2 database.

Flight label	Agency	Flight times	Median time of flight (UTC)	Dual-Doppler winds?	Max wind speed ($m\,s^{-1}$)
A	USAF	0316–1215 UTC 30 Aug	0801	No	51, category 3
B	NOAA P-3	1320–2245 UTC 30 Aug	1945	Yes	56, category 3
C	USAF	0353–1153 UTC 31 Aug	0803	No	59, category 4
D1	NOAA P-3	1455–2140 UTC 31 Aug	2003	Yes	64, category 4
D2	USAF	1615–2348 UTC 31 Aug	2003	No	64, category 4
E	USAF	0345–1154 UTC 1 Sep	0803	No	62, category 4
F1	NOAA P-3	1415–2300 UTC 1 Sep	2020	Yes	62, category 4
F2	USAF	1517–0043 UTC 1–2 Sep	2020	No	62, category 4
G	USAF	0251–1249 UTC 2 Sep	0843	No	64, category 4
H1	USAF	1051–2154 UTC 2 Sep	1939	No	59, category 4
H2	NOAA P-3	1510–2350 UTC 2 Sep	1939	Yes	59, category 4

produced a three-dimensional gridded (swath) analysis (Reasor et al. 2009; Rogers et al. 2015). These swath analyses were then transformed into cylindrical coordinates with a 1° azimuthal and 2-km radial resolution, which allowed for creation of radius versus height profiles extending out to 150 km and up to 15 km. In the swath analyses and radius–height cross sections, data included vertical and horizontal winds and reflectivity (Rogers et al. 2012).

Vertical wind shear data every six hours were obtained from the Statistical Hurricane Intensity Prediction Scheme (SHIPS). Shear is calculated in SHIPS as the magnitude difference between 850- and 200-hPa wind vectors, averaged over a 0–500-km radius from the vortex center (DeMaria et al. 2005). In this paper, the shear vector is the direction *from* which the shear is pointing (i.e., 270° is westerly wind shear). Several other environmental parameters (see Table 3) were also obtained from SHIPS. ERA-Interim analyses (Dee et al. 2011) were used to obtain upper-tropospheric wind and vorticity fields at 0.7° horizontal resolution.

3. Results

a. *Time series of eyewall replacement cycles in Hurricane Frances*

The ARCHER ring profile scores in Hurricane Frances from 27 August to 4 September are shown in a Hovmöller diagram in Fig. 1. On the right-hand side of the figure is a sequence of horizontal bars that indicate when microwave images were available for analysis. This was a well observed storm in the frequency of microwave data.

Table 2 details the evolution of the 0–500-km shear direction and magnitude, and the associated ERC state

TABLE 2. Evolution of the Hurricane Frances maximum wind speed ($m\,s^{-1}$), vertical shear magnitude ($m\,s^{-1}$), and direction (°) from the SHIPS database. Shear values represent the average value over 500 km from the storm center. A shear direction of 270° is *from* the west.

Time and date	ERC state	Shear direction	Shear magnitude ($m\,s^{-1}$)
0000 UTC 28 Aug 2004	ERC0 contracting	126°	2.4
1200 UTC 28 Aug 2004	ERC0 contracting	182°	2.3
0000 UTC 29 Aug 2004	ERC0 contracting	167°	4.2
1200 UTC 29 Aug 2004	ERC0 contracting	204°	7.2
0000 UTC 30 Aug 2004	ERC0 contracting	214°	5.3
1200 UTC 30 Aug 2004	ERC0 reaches storm core, ERC1 begins	159°	4.9
0000 UTC 31 Aug 2004	ERC1 contracting	156°	3.1
1200 UTC 31 Aug 2004	ERC1 contracting	120°	5.0
0000 UTC 1 Sep 2004	ERC1 reaches storm core, ERC2 begins	106°	4.2
1200 UTC 1 Sep 2004	ERC2 contracting	159°	3.4
0000 UTC 2 Sep 2004	ERC2 contracting	272°	4.8
1200 UTC 2 Sep 2004	ERC2 contracting	263°	7.8
0000 UTC 3 Sep 2004	ERC2 dissipating; radius of hurricane force winds increased substantially	264°	8.7

as inferred from Fig. 1. The start of an ERC was defined using the ARCHER ring score with shading in the green/yellow colors. The end of an ERC was defined by the time of the smallest radius for maximum microwave return indicated by the red shading in the core (inside the 35-km radius). Although these color choices appear arbitrary, the onset of a secondary wind maximum and the development of an outer eyewall closely followed the onset of blue and green shading, as will be seen in later wind and satellite figures. The red inner maxima represented the smallest radius of a significant inner eyewall.

Three distinct eyewall replacement cycles occurred. The first, labeled ERC0, formed at 2100 UTC 27 August and contracted at a rate 0.4 m s^{-1} until 1500 UTC 31 August. Only the end of this ERC could be examined due to the lack of flight-level data prior to 30 August (Table 1). As is typical (SKR11), a secondary eyewall (part of ERC1) was already forming at the 70-km radius at 0600 UTC 30 August while the storm continued to intensify. This outer eyewall contracted at a rate of 1.2 m s^{-1} and ERC1 lasted until 0600 UTC 1 September. The outer eyewall that initiated ERC2 formed near 0000 UTC 1 September while ERC1 was still contracting, producing further strengthening of the storm. ERC2 also contracted at a rate of 1.2 m s^{-1} and reached the 20-km radius near 1800 UTC 2 September. Table 2 indicates that the vertical wind shear magnitude during Hurricane Frances was moderate through most of the period, averaging 5.7 m s^{-1}. The shear briefly increased in magnitude and became westerly late on 29 August but then decreased in magnitude slightly and turned to be from the east and southeast for 48 h, from 1200 UTC 30 August to 1200 UTC 1 September.

A Hovmöller diagram of azimuthally averaged flight-level, storm-relative tangential wind versus radius for the 11 flights listed in Table 1 is produced in Fig. 2. The evolution of this field followed that of Fig. 1, in that wind maxima aligned well with convective maxima, lending support to the ARCHER ring scores. A wind maximum reached the 20-km radius between 1500 and 1800 UTC 30 August as part of ERC0. A second wind maximum developed at the 25–30-km radii at 0600 UTC 1 September, part of ERC1. The wind maximum associated with ERC2 approached the 30-km radius near 1200 UTC 2 September. Starting at about 1200 UTC 1 September, the tangential circulation increased dramatically, as the 35 m s^{-1} contour expanded from about the 85-km radius to the 140-km radius by 1800 UTC 3 September.

SKR11 identified an additional eyewall cycle that formed at 1636 UTC 3 September that contracted until 1901 UTC 4 September. This last ERC was not clearly

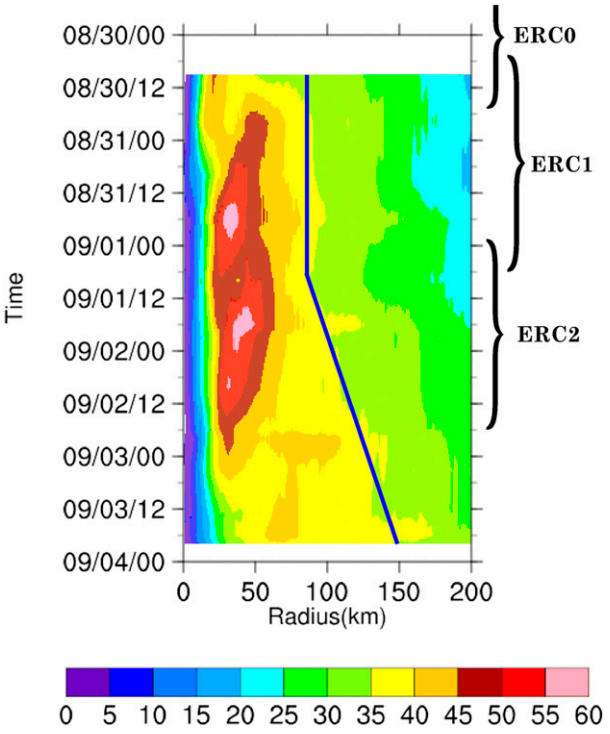

FIG. 2. Radius–time series of tangential velocity (m s^{-1}) averaged over all legs of each flight (P-3 and USAF, Table 2). Because flights did not begin until 30 Aug, this figure contains no fields from before that date. Brackets as in Fig. 1. The dark blue line segments indicate the dramatic radial expansion of hurricane-force winds during the third consecutive ERC.

evident in the ARCHER ring score (Fig. 1). It followed the three consecutive ERCs of interest in this paper only after a period of highly asymmetric convection. The symmetry, behavior, and timing of this event did not relate to the primary events of interest in this paper and are not examined further.

The azimuthal variations of the 3 ERCs are displayed using 89-GHz composite microwave images (Fig. 3). One key aspect of the figure is the near symmetry that existed within the 100-km radius during the period. Based on this symmetry of the precipitation field, it does not appear that asymmetric forcing played any significant role during the three ERCs.

Figure 3a (1709 UTC 30 August, coincident with flight B), provides evidence for all three eyewall replacement cycles. At this time were ERC0 at its innermost radius, ERC1 already well defined at the 50-km radius (Fig. 1), and an outer trailing spiral band was present near 200-km radius that had not yet symmetrized.

By 24 h later (Fig. 3b, during Flight D1), ERC1 had contracted and became the primary eyewall. No clear secondary eyewall was present at this time, but there

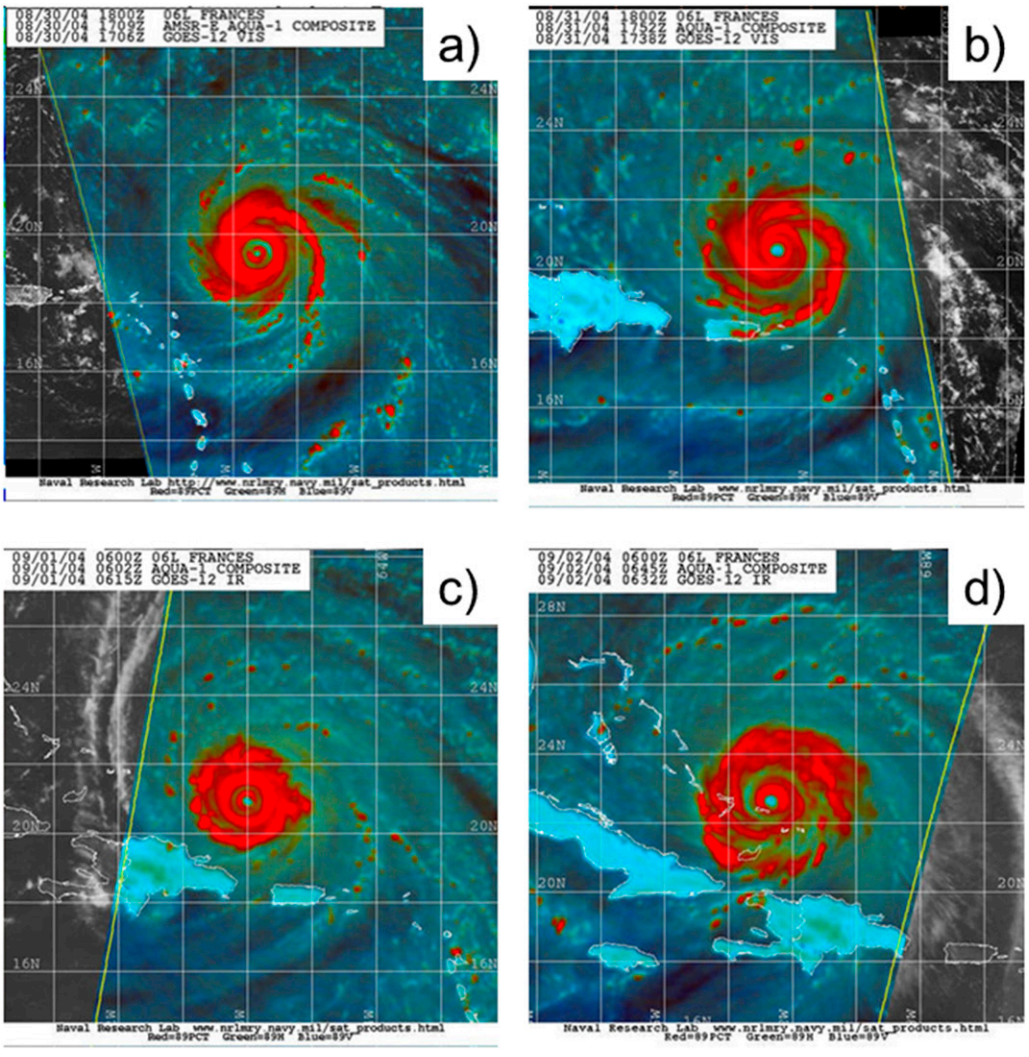

FIG. 3. 89-GHz composite microwave images at (a) 1709 UTC 30 Aug, (b) 1752 UTC 31 Aug, (c) 0602 UTC 1 Sep, and (d) 0645 UTC 2 Sep.

were well defined bands in the microwave at outer radii. By 0000 UTC 1 September (Fig. 3c), ERC1 was completing its contraction, ERC2 was well defined, and an additional outer band was found in all quadrants. Once again the two inner eyewalls were close to axisymmetric.

ERC2 reached the 20-km radius at 0600 UTC 2 September (Fig. 3d) while remaining nearly symmetric. Additional bands of convection developed about 200 km from the center. These might reflect the large increase in the radius of hurricane force winds shown in Fig. 2. These winds, which began to spin up on 1 September, would act to increase surface fluxes if the surface winds had a similar structure. The considerable symmetry in the microwave return in Fig. 3 suggests that the sheared eyewall studies of Didlake et al. (2017, 2018), Dai et al. (2017), and Dougherty et al. (2018) are not directly relevant to the Frances case.

b. *Flight-level data*

1) ERC0 AND ERC1 STRUCTURE

A sequence of azimuthally averaged flight-level, storm-relative tangential velocity is shown in the top panel of Fig. 4 for 30–31 August. Equivalent potential temperature θ_e is given in the bottom panel for P-3 flights only due to missing USAF data.

ERC0 can be seen in the aircraft data only in its final stages on 30 August, because there were no earlier flights. The first flight on 30 August (flight A; Table 1) had a sharp peak in the tangential wind at the 21-km radius and a weakly defined second wind maximum near

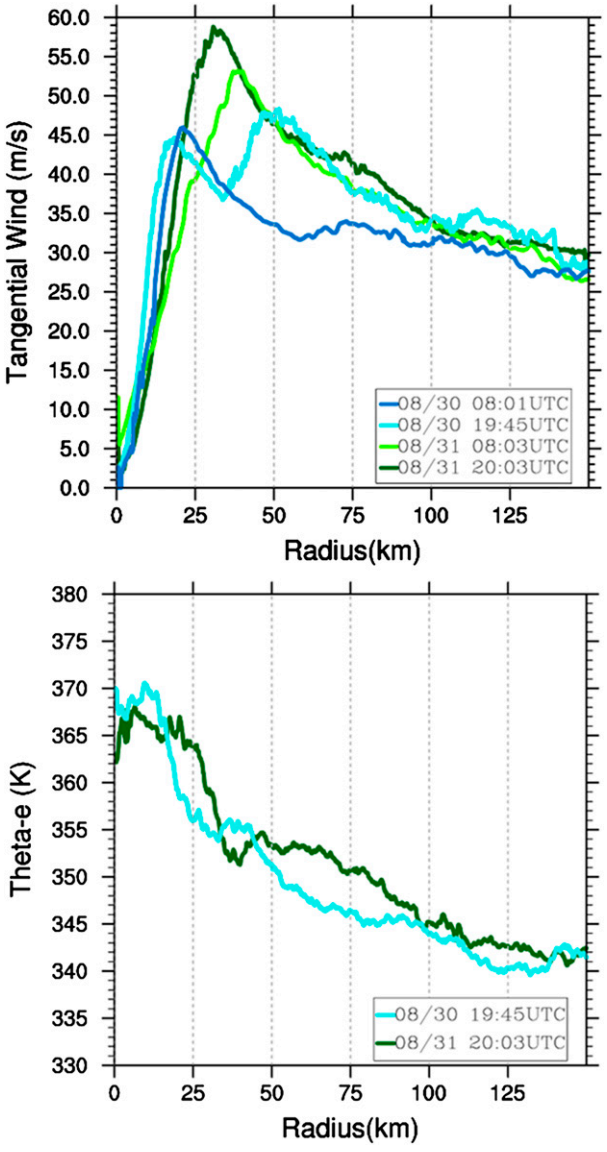

FIG. 4. (top) Azimuthally averaged, storm-relative tangential velocity spanning the completion of ERC0 through the life cycle of ERC1 from the flights in Table 1. (bottom) θ_e from the P-3 flights only; U.S. Air Force flights lacked the data for calculating θ_e.

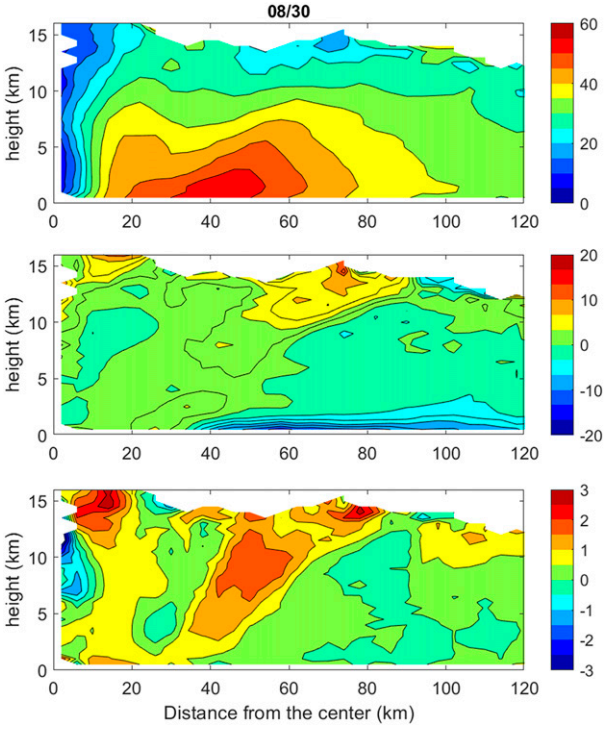

FIG. 5. Vertical profiles of dual-Doppler-derived storm-relative (top) tangential, (middle) radial, and (bottom) vertical velocity (all in m s^{-1}), azimuthally averaged over flight B (1945 UTC 30 Aug; see Table 2).

r = 70 km, which was approximately 3 times the radius of the inner wind maximum. This flight captured the end of ERC0 and the beginning of ERC1 (Table 1). Over the three subsequent flights, the inner eyewall of ERC0 dissipated while the outer eyewall of ERC1 contracted and became primary. Overall, the flight-level means exhibited a steady decrease in the radius of the outer eyewall, and a steady increase in the maximum wind speed, reaching nearly 60 m s^{-1} in the average of flights D1 and D2 (Table 1). This sequence fits a classic SKR11 eyewall cycle: inner eyewall dissipates, outer takes over, contracts, and becomes stronger than the original. Also consistent with SKR11, the new wind maximum was stronger and at a larger radius than the original. Despite these similarities, the outer eyewall wind speed for ERC1 surpassed the inner maximum in less than 12 h. This represents a sharp departure from the timing of SKR11, taking less than half as long as the composite ERC.

Figure 4 (bottom panel) shows flight-level θ_e for flights B and D1 (Table 1). Between 30 and 31 August, θ_e increased most dramatically between 50 and 90 km from the center, even as the wind maximum was contracting from r = 50 km to r = 30 km. There was a clear correspondence between radial θ_e gradients and the radius of maximum winds on both 30 and 31 August. This is consistent with thermal wind balance for saturated moist neutral ascent.

Figure 5 shows azimuthally averaged, dual-Doppler tangential, radial, and vertical motion from flight B late on 30 August. Two tangential wind maxima are evident; a strong outward-sloping maximum at r = 40 km, and a weaker more upright inner maximum at r = 20 km. Planetary boundary layer inflow exceeded 13 m s^{-1}, converging at the radius of the growing outer eyewall. Radial velocity was near zero through a deep layer in

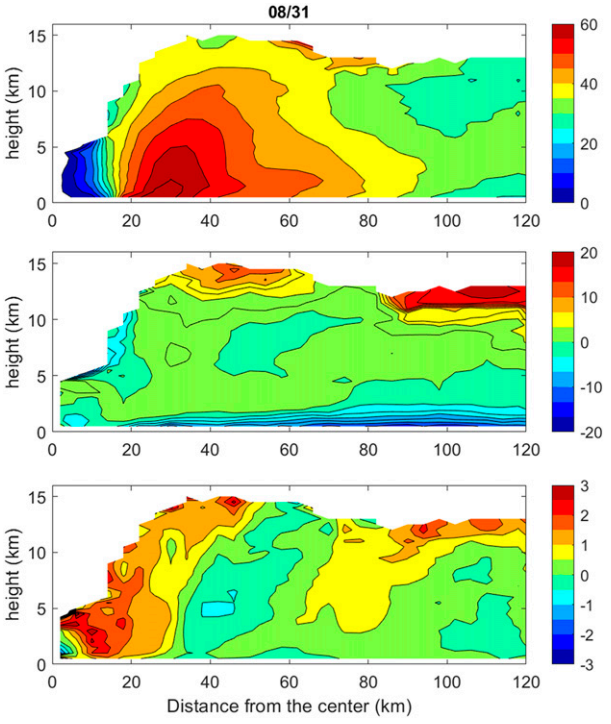

FIG. 6. As in Fig. 5, but for flight D1 (centered at 2003 UTC 31 Aug). ERC1 had reached completion with peak winds inside the 30-km radius, while the tangential wind accelerated at outer radii as ERC2 began.

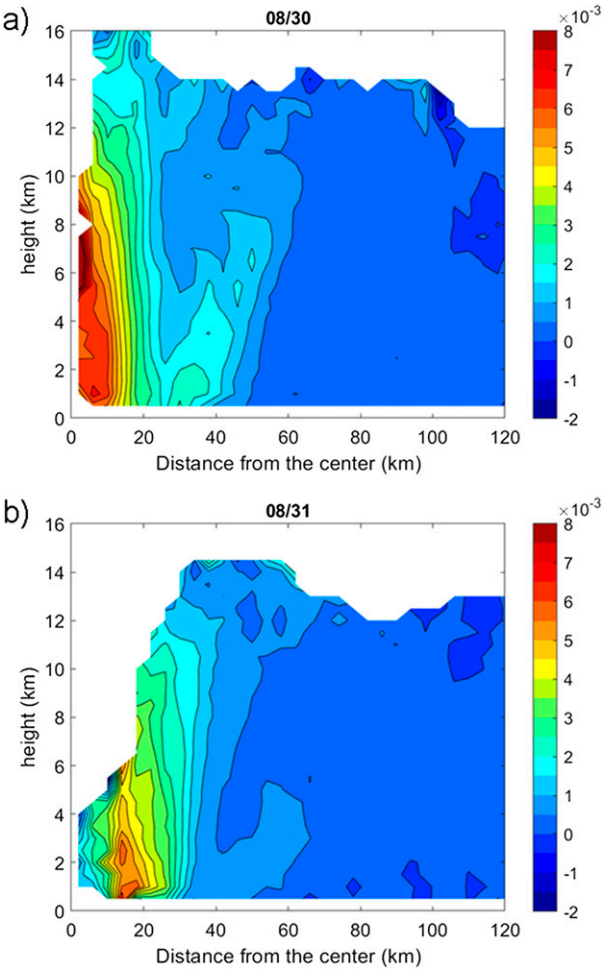

FIG. 7. Radial–vertical profiles of relative vorticity calculated from the dual-Doppler tangential winds in (a) Fig. 5 on 30 Aug, and (b) Fig. 6 on 31 Aug.

the vicinity of the decaying inner eyewall. In the upper troposphere, outflow approaching 20 m s^{-1} existed radially outside of the contracting secondary eyewall (part of ERC1). The vertical velocity displayed two updraft maxima: one with the dissipating inner eyewall at the 15-km radius, and a second sloped vertical velocity maximum that appeared as ERC1 began and extended through the depth of the troposphere. Between these two was a region of weak subsidence corresponding to the precipitation-free moat region seen in Fig. 3a. Weak inflow and subsidence occurred outside of the sloping secondary eyewall above the boundary layer. The broad, strong updraft in the outer eyewall (Fig. 5, bottom panel), which was accompanied by strong convection, was responsible for the increased radial θ_e gradients seen in the bottom panel of Fig. 4.

The azimuthally averaged dual-Doppler wind components for the P-3 flight (D1) during the final stage of ERC1 late on 31 August are given in Fig. 6. The tangential wind profile shows an inner maximum representing the primary eyewall inside the 30-km radius. Evidence of a broad weak outer maximum existed at about 3 times the RMW (also seen in Fig. 3), and was accompanied by upper-tropospheric outflow and deep sloping updrafts. A maximum in boundary layer inflow also existed outside this strengthening tangential wind maximum, which would soon become ERC2. This increase in secondary circulation outside the 60-km radius may be responsible for the increase in flight-level θ_e observed in the bottom panel of Fig. 4.

The relative vorticity fields for flights B and D2 on 30 and 31 August are shown in Fig. 7. A cyclonic vorticity maximum sloping outward from the 30-km radius over a 12-km layer was a striking aspect of the initial development of the eyewall with ERC1. The vorticity magnitude in the outer eyewall was relatively small, but Kepert (2013) noted that small vorticity maxima can create strong vertical circulations in an outer eyewall. One day later (Fig. 7b), the vorticity maximum within ERC2 already reached the 15-km radius. This rapid contraction emphasizes the unusual nature of Hurricane Frances timing of replacement cycles. Figure 7b also

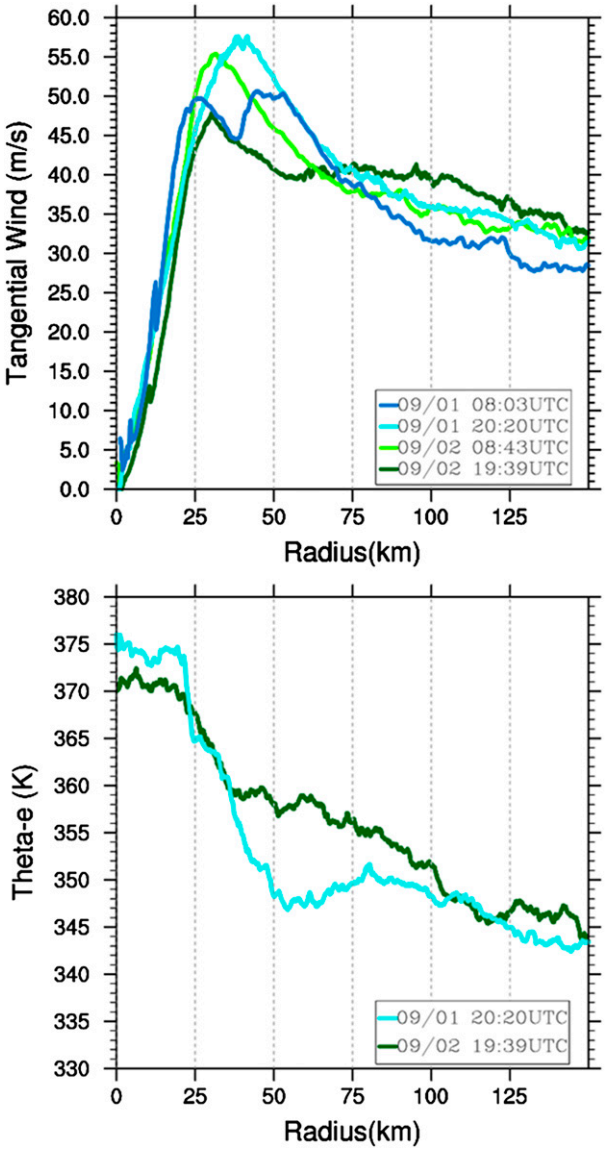

FIG. 8. Storm-relative (top) tangential velocity and (bottom) θ_e as in Fig. 4, but during the evolution of ERC2.

shows a shallow vorticity maximum near $r = 60$ km that represents the beginnings of the outer eyewall of ERC2.

2) ERC2 STRUCTURE

The evolution of flight-level tangential velocity and θ_e on 1 September is shown in Fig. 8. The black line (flight E) in Fig. 8 shows that the outer wind maximum with ERC2 had already become stronger than the inner maximum of ERC1. Once again this process occurred in only 12 h as compared to the longer secondary eyewall spinup time in SKR11 and Huang et al. (2012). After flight E, the outer eyewall contracted steadily late on 1 September through 2 September.

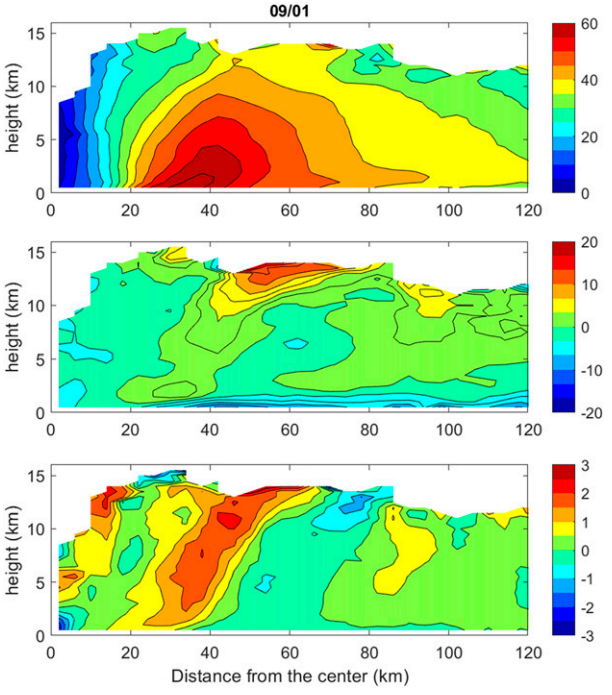

FIG. 9. As in Fig. 5, but for flight F1 (centered at 2020 UTC 1 Sep) in ERC2.

Unlike ERC1, the maximum wind speed weakened even as the eyewall contracted. This atypical behavior might relate to the increase in vertical wind shear by 1200 UTC 2 September (Table 1).

Figure 8 (bottom panel) shows flight-level θ_e for flights F1 and H2 (Table 1) on 1 and 2 September. The decrease in the radial gradient of θ_e is evident between the first and the second coincides with a decrease in the maximum wind and a broadening of the wind field during this period (top panel and Fig. 2). It seems likely that the dramatic expansion of the wind field on the second shown in Fig. 8a (see also below) produced the larger moist entropy from $r = 35$–100 km.

Dual-Doppler winds from the P-3 flights on 1 September (Fig. 9) and 2 September (Fig. 10) describe the evolution of ERC2. On 1 September, strong tangential wind peaked in the boundary layer at about the 35-km radius. Shallow inflow exceeding 12 m s^{-1} converged into the now dominant eyewall. The eyewall once again exhibited upper-level outflow approaching 20 m s^{-1}, as on 30 August, with weak downdrafts surrounding it. The outflow was accompanied by deep updrafts exceeding 2 m s^{-1} from just above the surface to the outflow layer. Within the decaying inner eyewall weak inflow in the low and midtroposphere and near-zero vertical velocity indicated its subsequent weakening.

The dual-Doppler winds for the P-3 flight late on 2 September (flight H2), 24 h after Fig. 9, are presented

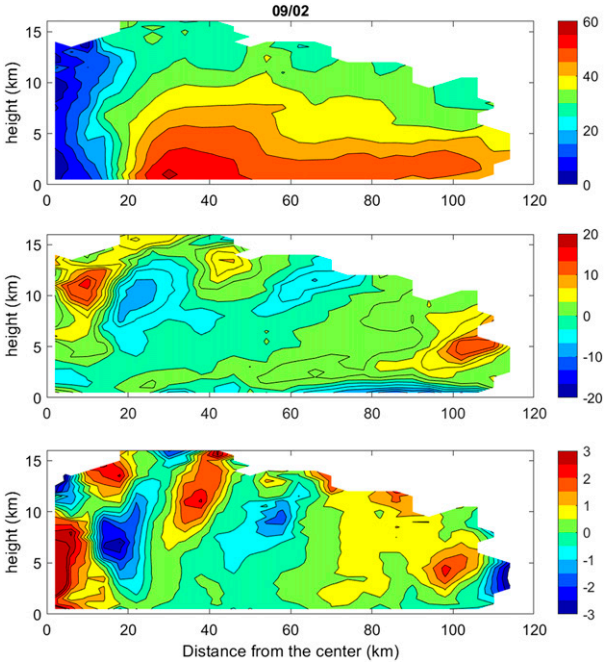

FIG. 10. As in Fig. 5, but for flight H2 (centered at 1939 UTC 2 Sep).

in Fig. 10. ERC2 winds peaked at the 28-km radius in the boundary layer. Strong convergence and upward motion existed in the primary eyewall, with sloping downdrafts radially outside of the sloping updrafts. This represented the completion of ERC2. The dramatic growth of hurricane-force winds beyond the 110-km radius shows clearly. One of the most striking aspects of Fig. 10 is the strong wavelike disturbance that shows in radial and especially vertical velocity. These perturbations display strong upward motion in the lower troposphere near $r = 0$, downward motion at 6–7-km height at $r = 20$ km, upward motion at 10-km height and $r = 40$ km, followed by subsidence at 50-km radii as the perturbation shifted downward with radius to the 9-km height.

Figure 11 shows relative vorticity during the evolution of ERC2. The inner eyewall of ERC1 (Fig. 11a) shows a strong vorticity maximum just inside the 20-km radius. The cyclonic vorticity actually leans inward with height, and is found inside the 10-km radius at $z = 7$ km. By the second, the vorticity maximum with ERC2 was well defined and extended through most of the troposphere inside $r = 20$ km. The wavelike disturbance does not seem to be reflected in the vorticity fields when compared to the radial and vertical velocity in Fig. 10; this might indicate that the disturbance is a gravity wave. The possible role of this feature in the dramatic expansion of hurricane force winds is uncertain and beyond the scope of this paper.

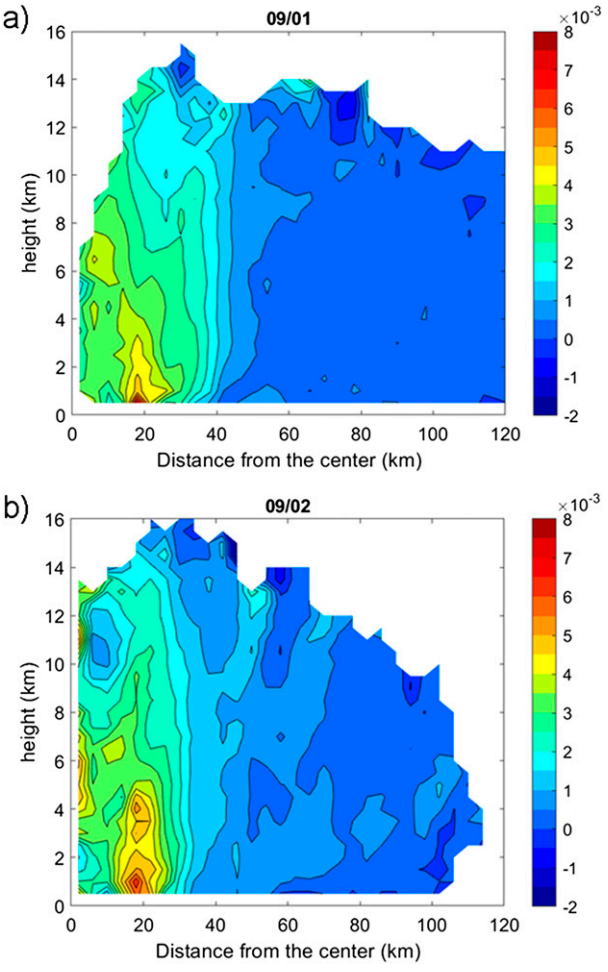

FIG. 11. Relative vorticity as in Fig. 7, but for (a) 1 Sep and (b) 2 Sep.

4. Discussion

Three primary factors will be addressed in this section: (i) the differences of Hurricane Frances from the KS09 and SKR11's ERC composites and other ERC studies; (ii) the possibility that Frances was an annular-like hurricane (Knaff et al. 2003); and (iii) whether there might be a connection of the two.

a. Comparison with KS09 and SKR11

Table 3 displays the KS09 composite parameters for "ERC/yes" and "ERC/no", obtained by Dougherty et al. (2018) based on values provided by J. Kossin (U. Wisconsin). Hurricane Frances resembled the "ERC/yes" rather than "ERC/no" composite for most variables, including storm intensity, MPI, their difference, latitude, mean brightness temperature for $r = 20$–120 km, and 850–200-hPa vertical wind shear magnitude. In that sense these were typical ERCs.

TABLE 3. Comparison of SKR11's "ERC/yes" and "ERC/no" SHIPS parameters with the average values from 0000 UTC 28 Aug–1800 UTC 2 Sep; T_b is brightness temperature. These values were produced by SKR11 and provided to Dougherty et al. (2018) by J. Kossin; thus the actual values are given in the Dougherty paper.

SHIPS parameters	"ERC/yes" from SKR11	"ERC/no" from SKR11	Hurricane Frances
Current intensity ($m\,s^{-1}$)	56.7	44.3	58.3
MPI ($m\,s^{-1}$)	68.2	59.3	69.5
MPI − intensity ($m\,s^{-1}$)	11.4	15.0	11.2
Latitude	21.7	27.0	19.8
Mean depth of 26°C water (m)	95.4	66.5	75.2
Mean 850-hPa $\mathbf{v}_\lambda$ over 600-km radius ($m\,s^{-1}$)	10.9	8.8	9.7
200-hPa mean zonal wind ($m\,s^{-1}$)	5.7	4.4	−6.2
850–200-hPa shear magnitude ($m\,s^{-1}$)	5.7	9.3	5.7
T_b averaged from r = 20 to 120 km (K)	−63.1	−54.7	−62.6

The unusual aspects of the ERCs in Frances were as follows:

1) Three consecutive overlapping eyewall replacement cycles occurred in Hurricane Frances. Of the 14 hurricanes examined by SKR11, only one other hurricane, Ivan (2004), had more than two overlapping ERC events. This made the ERC behavior in Frances unusual.
2) Once secondary wind maxima appeared, they rapidly, within 12 h, became stronger than the primary, more than twice as quickly as is typically observed.
3) Outflow in the upper troposphere above the secondary eyewalls exceeded 15 $m\,s^{-1}$, much stronger than is normally observed.
4) The depth of the 26° isotherm in the ocean was closer to the "ERC/no" value.
5) The mean 200-hPa zonal wind from SHIPS differed sharply from both "ERC/yes" and "ERC/no" composites: *easterly* zonal wind of 3.3 $m\,s^{-1}$ in Frances versus westerly wind of 5.5 $m\,s^{-1}$ for "ERC/yes." Not a single one of the "ERC/yes" cases in KS09 exhibited mean easterly flow at 200 hPa (see Fig. 6 in Dougherty et al. 2018).

ERA-Interim wind and absolute vorticity at 175 hPa averaged from 0000 UTC 28 August to 1800 UTC 2 September are shown in Fig. 12. The values at 200 hPa (not shown) closely resemble those at 175 hPa. The mean easterlies arose from a strong anticyclone that surrounded the storm through the entire period. This also created low inertial stability virtually in all quadrants in the upper troposphere, both on a daily basis (not shown) and in the mean. The low inertial stability reduced the resistance to convective outflow in all quadrants, and thus potentially led to the rapidly intensifying symmetric eyewalls seen in earlier figures. Strong upper outflow was present for each ERC event, as seen earlier in Figs. 5, 6, and 9. This synoptic environment does not represent the typical "ERC/yes" cases.

b. *Annular hurricanes*

Knaff et al. (2003, 2008) introduced the phenomenon of "annular hurricanes." These storms were stronger, maintained intensity longer, and weakened more slowly than average tropical cyclones. They had a distinct signature in infrared satellite pictures: large eyes (radii 32–64 km), thick eyewalls, and a relative lack of outer bands. These structures were rare, appearing in only about 4% of all hurricanes. Annular hurricanes experienced small vertical wind shear, often with a component from the east. Not a single annular hurricane had 200–800-km radii 200-hPa zonal wind from the

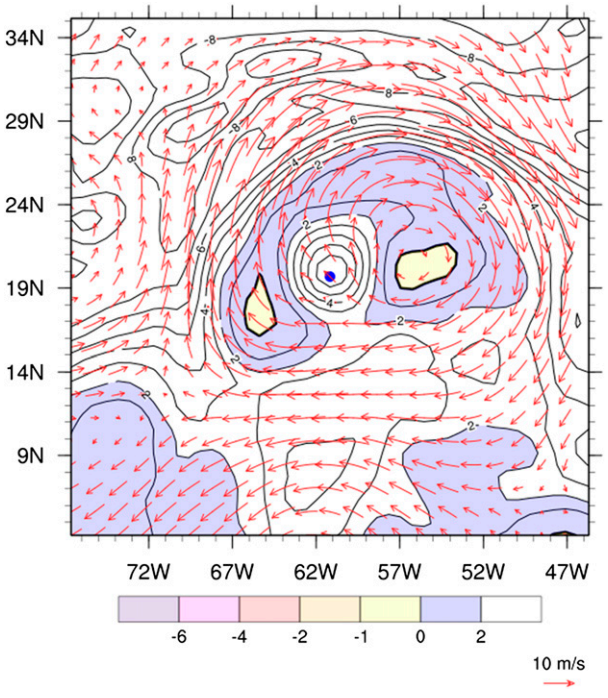

FIG. 12. Mean absolute vorticity and winds at 175 hPa from the ERA-Interim analysis for the period 0000 UTC 28 Aug–1800 UTC 2 Sep.

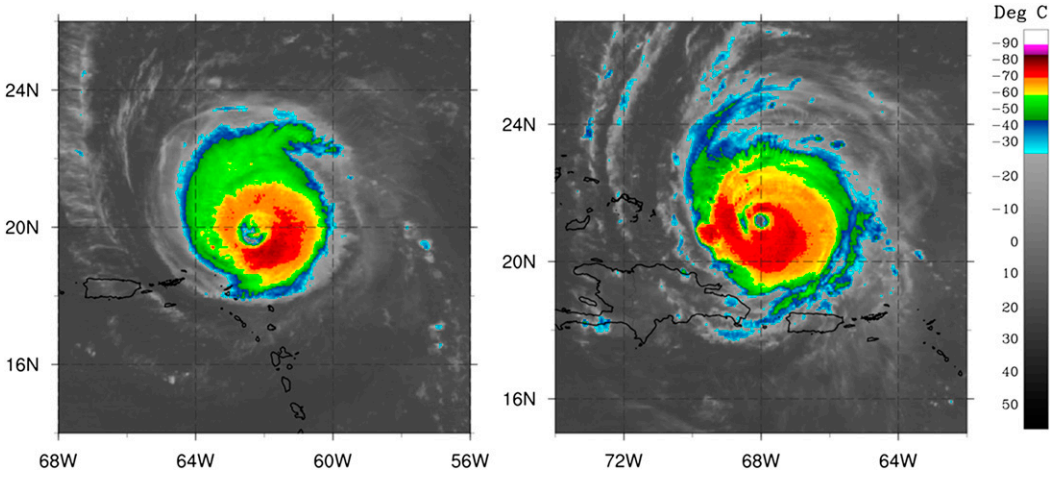

FIG. 13. Infrared images from (left) 0645 UTC 31 Aug and (right) 0645 UTC 1 Sep, both of which exhibited AHI > 0. The large eye, thick eyewall, and lack of outer bands show some signatures of annular hurricanes (Knaff et al. 2003).

west (Knaff et al. 2003). They also lacked interactions with environmental troughs as indicated by small azimuthal eddy flux convergence of angular momentum at upper levels.

Knaff et al. (2008) expanded the 2003 study to include more cases, and also measured a large number of environmental parameters surrounding the annular storms. They created an annular hurricane index (AHI) based upon these parameters to objectively evaluate the extent to which annular hurricane structure was met. The parameters involve wind, convection, SST, 200 hPa winds and temperature, and other factors [see Tables 1 and 3 in the paper by Knaff et al. (2008)]. If any one of the parameters failed to meet the cutoff criteria based on linear discriminant analysis, AHI was set equal to zero. The index values lie on a scale of 1–100, with larger values more likely to have annular structure, but even small nonzero values satisfy all annular criteria. Hurricane Frances had two periods where it contained nonzero AHI: 1) annular period 1, extending every 6 h from 0600 UTC 28 August to 1800 UTC 29 August (values ranging from 1 to 34); and 2) annular period 2 from 0600 UTC 31 August to 0600 UTC 2 September with one 6-h exception (values ranging from 1 to 37). The first annular period will not be addressed because no aircraft data exists for that time.

Knaff et al. (2003) argued for a special case where vertical wind shear that is weak and often from the east or southeast accompanied annular TCs. The wind shear in Frances (Table 2) was from the east or southeast for an extended period from 1200 UTC 30 August to 1200 UTC 1 September, which supports this view. Figure 13 shows infrared images for Frances at 0645 UTC 31 August and 0645 UTC 1 September where the "truck tire" thick eyewall and large eye resembled an annular hurricane. These times had nonzero AHI values and occurred during the long period of east–southeast shear. Because of the rarity of this phenomenon, the existence of these characteristics in Frances seems relevant to the evolution.

Figure 2 showed that annular period 2 followed the occurrence of multiple ERCs, as well as a dramatic increase in the radius of hurricane-force winds. Wang (2008) and Zhou and Wang (2009) simulated the development of an annular tropical cyclone using an idealized model. The annular stage developed after repeated eyewall cycles that produced a steadily larger circulation. As a result, the evolution of Hurricane Frances exhibited many aspects of Wang's (2008) circulation. Chu and Tan (2014), analogous to Knaff et al. (2003), found only 4% of Pacific typhoons became annular. This represents another unusual aspect of Hurricane Frances.

c. *Synthesis*

It is argued that internal forcing influenced the evolution of Hurricane Frances, because the outer eyewalls of both ERC1 and ERC2 formed at or near 3 times the RMW, implying a role for vortex Rossby waves. That being said, every storm in nature experiences some external forcing. In the case of Hurricane Frances, the TC encountered mean upper-tropospheric easterlies. The following sequence of events is proposed: major Hurricane Frances became embedded in a region of moderate easterly or southeasterly wind shear between 1200 UTC 30 August and late on 1 September, during which time two overlapping eyewall replacement cycles were initiated. The easterlies were equatorward of a

persistent upper anticyclone that was displaced slightly from the center. This environment produced low inertial stability (and some inertial instability) in all quadrants of the storm for a period of several days, similar to cases previously documented of regions of local inertial instability developing within the hurricane outflow layer (Alaka 1962; Black and Anthes 1971). More recently, Molinari and Vollaro (2014) showed the existence of symmetric instability in the outflow layer of major hurricane Ivan, a hurricane with multiple ERCs. Although such instability accelerates parcels both inward and outward, if the mean flow is outward, the acceleration is outward (Ooyama 1966). Strong outflow in the upper troposphere was evident in Figs. 5, 6, and 9, and was accompanied by deep updrafts extending above the 10-km level in the developing outer eyewalls. These strong updrafts contributed to the rapid strengthening of the outer wind maxima. The persistence of this low inertial stability environment supported repeated overlapping eyewall replacement cycles, which resulted in the development of a rare annular hurricane.

It is recommended that the ERC–annular hurricane relationship be further investigated. In addition, it remains uncertain what determines the number of eyewall replacement cycles in tropical cyclones, and how often upper-tropospheric forcing plays a role.

Acknowledgments. We benefited from substantive comments by Drs. Hugh Willoughby (Florida International University), Chris Rozoff (University of Wisconsin), and an anonymous reviewer. We thank Drs. Jim Kossin (University of Wisconsin), Mark DeMaria and Stephanie Stevenson (from the National Hurricane Center, NOAA), and John Knaff (NOAA, NESDIS) for beneficial email exchanges. Dr. Stevenson provided the annular hurricane index values in Hurricane Frances. This work is supported by NSF Grants AGS1453311 and AGS1636799.

REFERENCES

Abarca, S. F., and K. L. Corbosiero, 2011: Secondary eyewall formation in WRF simulations of Hurricanes Rita and Katrina (2005). *Geophys. Res. Lett.*, **38**, L07802, https://doi.org/10.1029/2011GL047015.

——, and M. T. Montgomery, 2014: Departures from axisymmetric balance dynamics during secondary eyewall formation. *J. Atmos. Sci.*, **71**, 3723–3738, https://doi.org/10.1175/JAS-D-14-0018.1.

——, and ——, 2015: Are eyewall replacement cycles governed largely by axisymmetric balance dynamics? *J. Atmos. Sci.*, **72**, 82–87, https://doi.org/10.1175/JAS-D-14-0151.1.

Alaka, M. A., 1962: On the occurrence of dynamic instability in incipient and developing hurricanes. *Mon. Wea. Rev.*, **90**, 49–58, https://doi.org/10.1175/1520-0493(1962)090<0049:OTOODI>2.0.CO;2.

Black, M. L., and H. E. Willoughby, 1992: The concentric eyewall cycle of Hurricane Gilbert. *Mon. Wea. Rev.*, **120**, 947–957, https://doi.org/10.1175/1520-0493(1992)120<0947:TCECOH>2.0.CO;2.

Black, P. G., and R. A. Anthes, 1971: On the asymmetric structure of the tropical cyclone outflow layer. *J. Atmos. Sci.*, **28**, 1348–1366, https://doi.org/10.1175/1520-0469(1971)028<1348:OTASOT>2.0.CO;2.

Chu, K., and Z.-M. Tan, 2014: Annular typhoons in the western North Pacific. *Wea. Forecasting*, **29**, 241–251, https://doi.org/10.1175/WAF-D-13-00060.1.

Corbosiero, K. L., J. Molinari, A. R. Aiyyer, and M. L. Black, 2006: The structure and evolution of Hurricane Elena (1985). Part II: Convective asymmetries and evidence for vortex Rossby waves. *Mon. Wea. Rev.*, **134**, 3073–3091, https://doi.org/10.1175/MWR3250.1.

Cotto, A., I. Gonzalez III, and H. E. Willoughby, 2015: Synthesis of vortex Rossby waves. Part I: Episodically forced waves in the inner waveguide. *J. Atmos. Sci.*, **72**, 3940–3957, https://doi.org/10.1175/JAS-D-15-0004.1.

Dai, Y., S. J. Majumdar, and D. S. Nolan, 2017: Secondary eyewall formation in tropical cyclones by outflow–jet interaction. *J. Atmos. Sci.*, **74**, 1941–1958, https://doi.org/10.1175/JAS-D-16-0322.1.

Dee, D. P., and Coauthors, 2011: The ERA-Interim reanalysis: Configuration and performance of the data assimilation system. *Quart. J. Roy. Meteor. Soc.*, **137**, 553–597, https://doi.org/10.1002/qj.828.

DeMaria, M., M. Mainelli, L. K. Shay, J. A. Knaff, and J. Kaplan, 2005: Further improvements to the Statistical Hurricane Intensity Prediction Scheme (SHIPS). *Wea. Forecasting*, **20**, 531–543, https://doi.org/10.1175/WAF862.1.

Didlake, A. C., Jr., and R. A. Houze Jr., 2011: Kinematics of the secondary eyewall observed in Hurricane Rita (2005). *J. Atmos. Sci.*, **68**, 1620–1636, https://doi.org/10.1175/2011JAS3715.1.

——, G. M. Heymsfield, P. D. Reasor, and S. R. Guimond, 2017: Concentric eyewall asymmetries in Hurricane Gonzalo (2014) observed by airborne radar. *Mon. Wea. Rev.*, **145**, 729–749, https://doi.org/10.1175/MWR-D-16-0175.1.

——, P. D. Reasor, R. F. Rogers, and W. C. Lee, 2018: Dynamics of the transition from spiral rainbands to a secondary eyewall in Hurricane Earl (2010). *J. Atmos. Sci.*, **75**, 2909–2929, https://doi.org/10.1175/JAS-D-17-0348.1.

Dougherty, E. M., J. Molinari, R. F. Rogers, J. A. Zhang, and J. P. Kossin, 2018: Hurricane Bonnie (1998): Maintaining intensity during high vertical wind shear and an eyewall replacement cycle. *Mon. Wea. Rev.*, **146**, 3383–3399, https://doi.org/10.1175/MWR-D-18-0030.1.

Gamache, J. F., and F. Marks Jr., 1997: Evaluation of a fully three-dimensional variational Doppler analysis technique. Preprints, *28th Conf. on Radar Meteorology,* Austin, TX, Amer. Meteor. Soc., 422–423.

Gonzalez, I., III, A. Cotto, and H. E. Willoughby, 2015: Synthesis of vortex Rossby waves. Part II: Vortex motion and waves in the outer waveguide. *J. Atmos. Sci.*, **72**, 3958–3974, https://doi.org/10.1175/JAS-D-15-0005.1.

Guinn, T. A., and W. H. Schubert, 1993: Hurricane spiral bands. *J. Atmos. Sci.*, **50**, 3380–3403, https://doi.org/10.1175/1520-0469(1993)050<3380:HSB>2.0.CO;2.

Huang, Y.-H., M. T. Montgomery, and C.-C. Wu, 2012: Concentric eyewall formation in Typhoon Sinlaku (2008). Part II: Axisymmetric dynamical processes. *J. Atmos. Sci.*, **69**, 662–674, https://doi.org/10.1175/JAS-D-11-0114.1.

Kepert, J. D., 2013: How does the boundary layer contribute to the eyewall replacement cycles in axisymmetric tropical

cyclones? *J. Atmos. Sci.*, **70**, 2808–2830, https://doi.org/10.1175/JAS-D-13-046.1.

Knaff, J. A., J. Kossin, and M. DeMaria, 2003: Annular hurricanes. *Wea. Forecasting*, **18**, 204–223, https://doi.org/10.1175/1520-0434(2003)018<0204:AH>2.0.CO;2.

——, T. A. Cram, A. B. Schumacher, J. P. Kossin, and M. DeMaria, 2008: Objective identification of annular hurricanes. *Wea. Forecasting*, **23**, 17–28, https://doi.org/10.1175/2007WAF2007031.1.

Kossin, J. P., and M. Sitkowski, 2009: An objective model for identifying secondary eyewall formation in hurricanes. *Mon. Wea. Rev.*, **137**, 876–892, https://doi.org/10.1175/2008MWR2701.1.

——, and M. DeMaria, 2016: Reducing operational hurricane intensity forecast errors during eyewall replacement cycles. *Wea. Forecasting*, **31**, 601–608, https://doi.org/10.1175/WAF-D-15-0123.1.

Molinari, J., and D. Vollaro, 1989: External influences on hurricane intensity. Part I: Outflow layer eddy angular momentum fluxes. *J. Atmos. Sci.*, **46**, 1093–1105, https://doi.org/10.1175/1520-0469(1989)046<1093:EIOHIP>2.0.CO;2.

——, and ——, 2014: Symmetric instability in the outflow layer of a major hurricane. *J. Atmos. Sci.*, **71**, 3739–3746, https://doi.org/10.1175/JAS-D-14-0117.1.

Montgomery, M. T., and R. J. Kallenbach, 1997: A theory for vortex Rossby-waves and its application to spiral bands and intensity changes in hurricanes. *Quart. J. Roy. Meteor. Soc.*, **123**, 435–465, https://doi.org/10.1002/qj.49712353810.

Nong, S., and K. Emanuel, 2003: A numerical study of the genesis of concentric eyewalls in hurricanes. *Quart. J. Roy. Meteor. Soc.*, **129**, 3323–3338, https://doi.org/10.1256/qj.01.132.

Ooyama, K., 1966: On the stability of the baroclinic circular vortex: A sufficient criterion for instability. *J. Atmos. Sci.*, **23**, 43–53, https://doi.org/10.1175/1520-0469(1966)023<0043:OTSOTB>2.0.CO;2.

Pendergrass, A. G., and H. E. Willoughby, 2009: Diabatically induced secondary flows in tropical cyclones. Part I: Quasi-steady forcing. *Mon. Wea. Rev.*, **137**, 805–821, https://doi.org/10.1175/2008MWR2657.1.

Reasor, P. D., M. D. Eastin, and J. F. Gamache, 2009: Rapidly intensifying Hurricane Guillermo (1997). Part I: Low-wavenumber structure and evolution. *Mon. Wea. Rev.*, **137**, 603–631, https://doi.org/10.1175/2008MWR2487.1.

Rogers, R. F., S. Lorsolo, P. Reasor, J. Gamache, and F. Marks, 2012: Multiscale analysis of tropical cyclone kinematic structure from airborne Doppler radar composites. *Mon. Wea. Rev.*, **140**, 77–99, https://doi.org/10.1175/MWR-D-10-05075.1.

——, P. D. Reasor, and J. A. Zhang, 2015: Multiscale structure and evolution of Hurricane Earl (2010) during rapid intensification. *Mon. Wea. Rev.*, **143**, 536–562, https://doi.org/10.1175/MWR-D-14-00175.1.

Rozoff, C. M., D. S. Nolan, J. P. Kossin, F. Zhang, and J. Fang, 2012: The roles of an expanding wind field and inertial stability in tropical cyclone secondary eyewall formation. *J. Atmos. Sci.*, **69**, 2621–2643, https://doi.org/10.1175/JAS-D-11-0326.1.

Shapiro, L. J., and H. E. Willoughby, 1982: The response of balanced hurricanes to local sources of heat and momentum. *J. Atmos. Sci.*, **39**, 378–394, https://doi.org/10.1175/1520-0469(1982)039<0378:TROBHT>2.0.CO;2.

Sitkowski, M., J. P. Kossin, and C. M. Rozoff, 2011: Intensity and structure changes during hurricane eyewall replacement cycles. *Mon. Wea. Rev.*, **139**, 3829–3847, https://doi.org/10.1175/MWR-D-11-00034.1.

Terwey, W. D., and M. T. Montgomery, 2008: Secondary eyewall formation in two idealized, full-physics modeled hurricanes. *J. Geophys. Res.*, **113**, D12112, https://doi.org/10.1029/2007JD008897.

Vigh, J. L., and Coauthors, 2018: FLIGHT+: The extended flight level dataset for tropical cyclones (version 1.3). Tropical Cyclone Data Project, National Center for Atmospheric Research, Research Applications Laboratory, Boulder, CO, accessed 28 June 2018, https://doi.org/10.5065/D6WS8R93.

Wang, Y., 2008: Structure and formation of an annular hurricane simulated in a fully compressible, nonhydrostatic model: TCM4. *J. Atmos. Sci.*, **65**, 1505–1527, https://doi.org/10.1175/2007JAS2528.1.

Willoughby, H. E., J. A. Clos, and M. G. Shoreibah, 1982: Concentric eye walls, secondary wind maxima, and the evolution of the hurricane vortex. *J. Atmos. Sci.*, **39**, 395–411, https://doi.org/10.1175/1520-0469(1982)039<0395:CEWSWM>2.0.CO;2.

Wimmers, A. J., J. Kossin, and D. Herndon, 2018: Improved eyewall replacement cycle forecasting using a modified microwave-based algorithm. *33rd Conf. on Hurricanes and Tropical Meteor.*, Jacksonville, FL, Amer. Meteor. Soc., 10D.2, https://ams.confex.com/ams/33HURRICANE/meetingapp.cgi/Paper/339864.

——, and C. S. Velden, 2016: Advancements in objective multisatellite tropical cyclone center fixing. *J. Appl. Meteor. Climatol.*, **55**, 197–212, https://doi.org/10.1175/JAMC-D-15-0098.1.

——, D. Herndon, and J. Kossin, 2017: Improved eyewall replacement cycle forecasting using ARCHER-a modified microwave-based algorithm (year 2). NOAA Joint Hurricane Testbed Rep., 26 pp., https://www.ofcm.gov/meetings/TCORF/ihc17/Session_09/9-2%20archer-erc_web.pdf.

Wu, C.-C., S. N. Wu, and S. F. Abarca, 2016: The role of convective heating in tropical cyclone eyewall ring evolution. *J. Atmos. Sci.*, **73**, 319–330, https://doi.org/10.1175/JAS-D-15-0085.1.

Zhou, X., and B. Wang, 2009: From concentric eyewall to annular hurricane: A numerical study with the cloud-resolved WRF model. *Geophys. Res. Lett.*, **36**, L03802, https://doi.org/10.1029/2008GL036854.